Inorganic Chemistry

pubs.acs.org/IC

Communication

Yellow Emissive $CsCu_2I_3$ Nanocrystals Induced by Mn^{2+} for High-Resolution X-ray Imaging

Lingfeng Li, Zutao Fan, Jie Zhang, Dianyuan Fan, Xiaogang Liu, and Yu Wang*

Cite This: *Inorg. Chem.* 2023, 62, 19848−19855

Read Online

ACCESS | Metrics & More | Article Recommendations | Supporting Information

ABSTRACT: Recently, low-dimensional copper(I)-based perovskite or derivatives have gained extensive attention in scintillator applications because of their environmental friendliness and good stabilities. However, the unsatisfactory scintillation performance and complex fabrication processes hindered their practical applications. Herein, efficient yellow emissive $CsCu_2I_3$ nanocrystals (NCs) were successfully prepared via a simple Mn^{2+}-assisted hot-injection method. The added Mn^{2+} effectively induced the phase transformation from $Cs_3Cu_2I_5$ to $CsCu_2I_3$, leading to the preparation of single-phase $CsCu_2I_3$ NCs with few defects and a high fluorescence performance. The as-prepared "optimal $CsCu_2I_3$ NCs" exhibited superior photoluminescence (PL) performance with a record-high PL quantum yield (PLQY) of 61.9%. The excellent fluorescence originated from the radiative recombination of strongly localized one-dimension (1D) self-trapped excitons (STEs), which was systematically investigated via the wavelength-dependent PL excitation, PL emission, and temperature-dependent PL spectra. These $CsCu_2I_3$ NCs also exhibited outstanding X-ray scintillation properties with a high light yield (32000 photons MeV^{-1}) and an ultralow detection limit (80.2 nGy_{air} s^{-1}). Eventually, the $CsCu_2I_3$ NCs scintillator film achieved an ultrahigh (16.6 lp mm^{-1}) spatial resolution in X-ray imaging. The $CsCu_2I_3$ NCs also exhibited good stabilities against X-ray irradiation, heat, and environmental storage, indicating their great application potential in flexible X-ray detection and imaging.

Downloaded via NATL UNIV OF SINGAPORE on April 24, 2024 at 10:24:51 (UTC).
See https://pubs.acs.org/sharingguidelines for options on how to legitimately share published articles.

1. INTRODUCTION

Scintillators, which can convert high-energy photons (such as X-ray photons) into ultraviolet or visible ones, play significant roles in many fields, including medical imaging, nondestructive testing, security inspection and industrial control.[1−6] Traditionally, CsI(Tl), $Lu_{1.8}Y_{0.2}SiO_5$:Ce (LYSO), $Bi_4Ge_3O_{12}$ and $LaBr_3$:Ce are the most used scintillators.[7,8] However, these scintillators exhibit several disadvantages, such as complex fabrication processes, high preparation cost, low light yield (LY) and poor stability. For example, CsI(Tl) films are produced via time-consuming thermal deposition.[9] LYSO bulk crystals are fabricated at high temperatures (>1500 °C) via the Czochralski method, resulting in high preparation costs.[10,11] In addition, the obtained bulk scintillators are inherently brittle, which limits their applications in flexible X-ray detection and imaging. $Bi_4Ge_3O_{12}$ exhibits an ultralow LY of 9000 photons MeV^{-1}.[12] Thus, it is urgent to develop new scintillators with easy preparation, low fabrication cost, solution-processability, high LY and good stability.[13,14] Lead-halide perovskite nanocrystals (NCs) were the first reported scintillators prepared via a facile solution strategy. They exhibited several exciting scintillation properties, including fast scintillation response, strong X-ray absorption, ultrasensitive X-ray sensing and tunable radioluminescence (RL).[15−23] However, their practical applications were hindered by their relatively low LY (21000 photons MeV^{-1}), poor environmental stability and lead toxicity.[17,24,25]

Recently, low-dimensional Cu(I)-based perovskite or derivatives have attracted extensive attention as scintillators due to their high PL quantum yield (PLQY), easy fabrication, good stability and nontoxicity.[26−34] For example, Tang's group synthesized one-dimensional (1D) perovskite Rb_2CuCl_3 with ultrahigh PLQY (99.4%) and good stability via a facile solution method. The Rb_2CuCl_3 also demonstrates an acceptable LY of 16600 photons MeV^{-1} under X-ray irradiation.[26] Besides, Tang's group also fabricated a stable 1D perovskite Rb_2CuBr_3 scintillator with ultrahigh LY (97000 photons MeV^{-1}).[35] Nevertheless, the high natural radioactivity of Rb in Rb_2CuBr_3 and Rb_2CuCl_3 dramatically limits their practical applications.

Via replacing Rb^+ ions with Cs^+, many other low-dimensional Cu(I)-based perovskite or derivatives have also been reported, including $CsCu_9X_{10}$ (X = Cl, Br, and I), $CsCu_4X_5$, $CsCu_2X_3$, $CsCuX_2$, $Cs_3Cu_2X_5$ (X = Cl, I) and Cs_2CuX_3.[36−38] Among these compounds, zero-dimensional (0D) $Cs_3Cu_2I_5$ has received particular attention and has been reported as an efficient scintillator. The deficiency is the long fluorescence lifetime (~1500 ns) of 0D $Cs_3Cu_2I_5$, which is not favorable for fast X-ray detection and imaging.[29] In comparison, 1D $CsCu_2I_3$ features a much shorter fluorescence lifetime (~50 ns).[37] In addition, the advantages of 1D $CsCu_2I_3$ in scintillation applications include: (i) strong electron−phonon coupling to form self-trapped excitons (STEs) for radioluminescence; (ii) unique 1D crystal structure to ensure efficient separation and stable existence of excitons; (iii) no radiation background to ensure a low X-ray

Received: October 21, 2023
Revised: November 20, 2023
Accepted: November 21, 2023
Published: November 30, 2023

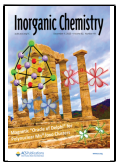

© 2023 American Chemical Society

https://doi.org/10.1021/acs.inorgchem.3c03724
Inorg. Chem. 2023, 62, 19848−19855

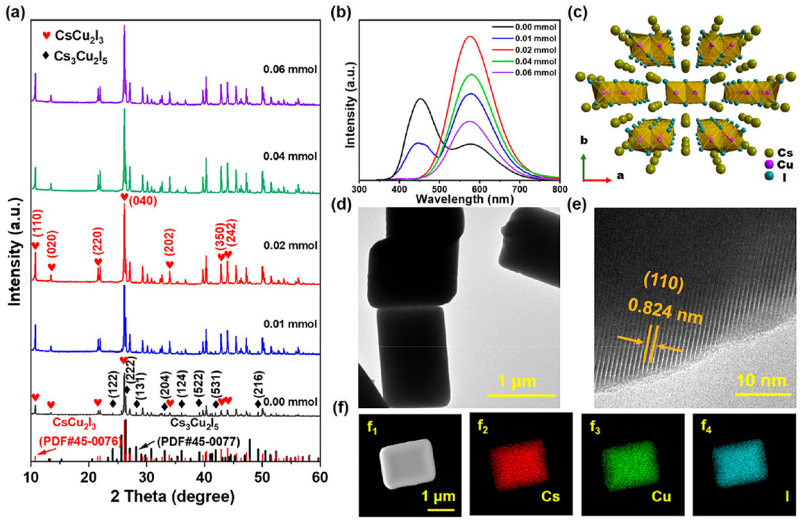

Figure 1. (a) XRD patterns and (b) PL spectra of the $CsCu_2I_3$ (or $Cs_3Cu_2I_5$) NCs synthesized with different additive amount of Mn^{2+}; (c) Crystal structure (a top view), (d) TEM image, (e) HRTEM image and (f) EDX mapping of Cs, Cu, I elements of the optimal $CsCu_2I_3$ NCs. A top view of the $CsCu_2I_3$ NCs exhibits the double chains of $[Cu_2I_6]^{4-}$ isolated by Cs atoms.

detection limit and (iv) good stability, etc.[39,40] Whereas, there are few reports about $CsCu_2I_3$ as a scintillator, due to its unsatisfied X-ray scintillation performance. Moreover, the reported methods for preparing 1D $CsCu_2I_3$ are usually complex and time-consuming, such as the Bridgman method, inverse solvent recrystallization method and inverse temperature crystallization method.[37,41,42] Thus, it is of significance to synthesize an efficient $CsCu_2I_3$ scintillator via a simple and efficient (time-saving) route.

Herein, a facile Mn^{2+}-assisted hot-injection route was adopted to synthesize efficient yellow emissive $CsCu_2I_3$ NCs. It is found that adding a small amount of Mn^{2+} could effectively induce the phase transformation from $Cs_3Cu_2I_5$ to $CsCu_2I_3$ during the synthesis process. Via optimizing the additive amount of Mn^{2+}, the "optimal $CsCu_2I_3$ NCs" with single-phase purity and few defects were obtained when the addition amount of Mn^{2+} was 0.02 mmol. The as-obtained optimal $CsCu_2I_3$ NCs exhibited outstanding photoluminescence (PL) performance with a record-high PLQY of 61.9%. The excellent fluorescence performance of the optimal $CsCu_2I_3$ NCs was attributed to the strongly localized 1D STEs emission, which was systematically investigated by the wavelength-dependent PL excitation, PL emission, and temperature-dependent PL spectra. Superior scintillation properties (a high LY of 32000 photons MeV^{-1} and an ultralow X-ray detection limit of 80.2 nGy_{air} s^{-1}) were also achieved for the optimal $CsCu_2I_3$ NCs. Eventually, the $CsCu_2I_3$ NCs scintillator film demonstrated an ultrahigh spatial resolution (16.6 lp mm^{-1}) in X-ray imaging. These $CsCu_2I_3$ NCs also displayed good stabilities against X-ray irradiation, heat, and environmental storage, suggesting their huge application potential in flexible X-ray detection and imaging.

2. EXPERIMENTAL SECTION

2.1. Materials. Cs_2CO_3 (99.9%), CuI (99.95%), Mn-$(CH_3COO)_2{\cdot}4H_2O$ (99.99%), Oleic acid (OA, 90%), 1-Octadecene (ODE, tech.90%) Oleylamine (OAm, 80−90%) and *n*-hexane (HPLC, ≥ 98%) were all purchased from Shanghai Aladdin Bio-Chem Technology Co., LTD and were used as received.

2.2. Synthesis of Cs-Oleate (CsOA) Precursor. The CsOA precursor was synthesized via a previous route.[43] Briefly, Cs_2CO_3 (1 mmol), OA (2 mL) and ODE (10 mL) were put into a three-neck flask (100 mL), and the mixture was kept stirring at 120 °C for 60 min under vacuum. The CsOA precursor was obtained when the solution became transparent. After that, the as-obtained CsOA precursor was kept at 100 °C in a N_2 atmosphere for the subsequent preparation of $CsCu_2I_3$ NCs.

2.3. Synthesis of $CsCu_2I_3$ NCs. A modified hot-injection method was adopted to prepare the $CsCu_2I_3$ NCs. Briefly, CuI (2 mmol), $Mn(CH_3COO)_2{\cdot}4H_2O$ (0.00 mmol, 0.01 mmol, 0.02 mmol, 0.04 mmol, 0.06 mmol), OAm (1.5 mL), OA (0.5 mL) and ODE (10 mL) were put into a three-neck flask (100 mL), and the reaction system was kept stirring at 120 °C for 60 min under vacuum. After all the reactants were dissolved, the reaction system was heated to 150 °C under an N_2 atmosphere. Subsequently, the CsOA solution (6 mL) was injected into the flask quickly, and a white precipitate was formed immediately. Five min later, an ice−water bath was used to cool the reaction system to room temperature, and the perovskite NCs were obtained (as displayed in Figure S1). Then, the as-obtained NCs were washed/purified with *n*-hexane and centrifuged at 10000 rpm for 10 min. The washing/filtering was repeated several times. Finally, the collected NCs were dried under a vacuum for 24 h at 70 °C for further characterization.

2.4. $CsCu_2I_3$ NCs Scintillator Film and Characterization Methods. Detailed descriptions of the preparation of the $CsCu_2I_3$ NCs scintillator film, and the characterization methods are presented in the Supporting Information.

3. RESULTS AND DISCUSSION

3.1. Crystal Structure and Morphology Characterization. To investigate the crystal structure and phase composition of the prepared perovskite NCs, X-ray diffraction (XRD) characterization was carried out for different samples. As shown in Figure 1a, two groups of XRD peaks can be observed, which are ascribed to orthorhombic $CsCu_2I_3$ (PDF#45-0076) and $Cs_3Cu_2I_5$ (PDF#45-0077), respectively, demonstrating the coexistence of $CsCu_2I_3$ and $Cs_3Cu_2I_5$ without Mn^{2+} addition in the synthesis process. With the addition of Mn^{2+} gradually

https://doi.org/10.1021/acs.inorgchem.3c03724
Inorg. Chem. 2023, 62, 19848−19855

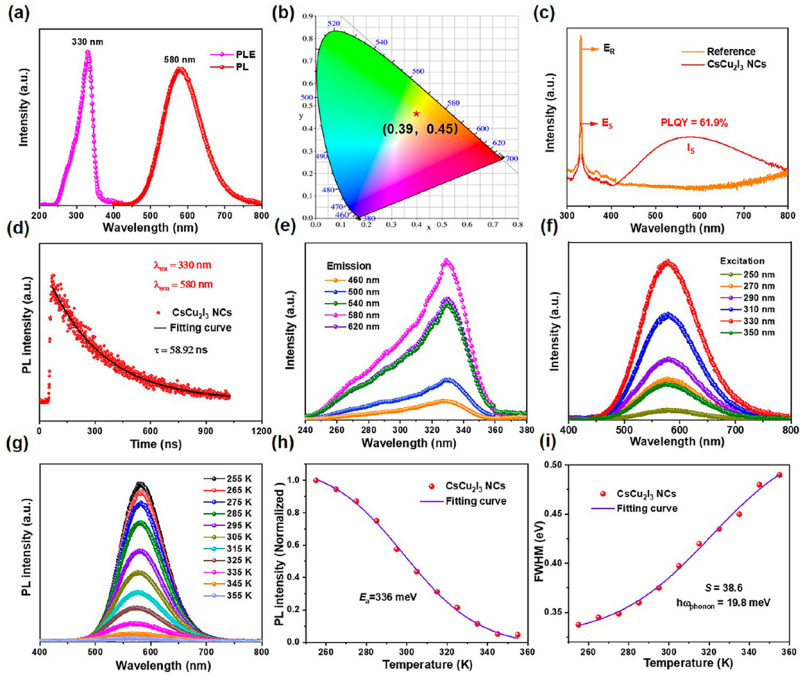

Figure 2. PL characterizations of the optimal $CsCu_2I_3$ NCs. (a) Excitation and emission spectra. (b) CIE 1931 color coordinates. (c) Absolute PL quantum yield (PLQY) result. (d) PL decay curve. (e) Wavelength-dependent PL excitation spectra. (f) Wavelength-dependent PL emission spectra. (g) Temperature-dependent PL spectra. (h) Fitting curve of the PL intensity versus the temperature. (i) Fitting curve of the FWHM versus the temperature.

increasing to 0.02 mmol, the characteristic XRD peaks of $Cs_3Cu_2I_5$ disappear, and only those of $CsCu_2I_3$ exist, indicating the successful preparation of "pure-phase $CsCu_2I_3$ NCs". It has been reported that dopants can destroy the balance of the Cs−Cu−I system and induce phase transformation from $Cs_3Cu_2I_5$ to the more stable $CsCu_2I_3$. However, the phase transformation process will not be reversed under the same circumstance because the impurities could not induce $CsCu_2I_3$ to $Cs_3Cu_2I_5$.[44] Therefore, in this work, the role of the added Mn^{2+} is deemed to be conversion revulsive, which induces the phase transformation from $Cs_3Cu_2I_5$ to $CsCu_2I_3$, thus resulting in the fabrication of pure-phase $CsCu_2I_3$ NCs. No new species but only the single $CsCu_2I_3$ phase exists when the amount of Mn^{2+} is 0.02 mmol or more. Besides, no diffraction peaks attributed to precursors (e.g., CsOA, CuI and $Mn(CH_3COO)_2$) appear, demonstrating the complete reaction of precursors to form the single-phase $CsCu_2I_3$.[45] Accordingly, the PL result is consistent with the XRD characterization. As shown in Figure 1b, the PL spectrum of the NCs prepared without Mn^{2+} additive displays dual emission peaks at 445 and 580 nm, corresponding to the characteristic PL spectra of $Cs_3Cu_2I_5$ and $CsCu_2I_3$ NCs, respectively.[44] With the amount of Mn^{2+} gradually increasing to 0.02 mmol, the PL intensity of the peak attributed to $Cs_3Cu_2I_5$ (445 nm) gradually weakens to disappear. Meanwhile, the PL intensity of the peak attributed to $CsCu_2I_3$ (580 nm) gradually increases. However, when the amount of Mn^{2+} was further increased to 0.04 mmol or more, the PL intensity of the pure-phase $CsCu_2I_3$ NCs gradually decreases. This could be attributed to the fact that too much Mn^{2+} can destroy the surface of $CsCu_2I_3$ NCs via detaching the OA/OAm ligands off the NCs surface, leading to the exposure of more surface defects, thus causing nonradiative recombination of excitons. Thus, pure-phase $CsCu_2I_3$ NCs with fewer defects are obtained when Mn^{2+} is 0.02 mmol. Hereafter, the $CsCu_2I_3$ NCs synthesized with 0.02 mmol of Mn^{2+} are designated as "optimal $CsCu_2I_3$ NCs". It can be seen from the crystal structure illustration (Figure 1c), the optimal $CsCu_2I_3$ NCs exhibit a 1D structure, in which edge-sharing and face-sharing Cu^+I_4 tetrahedra form double chains of $[Cu_2I_6]^{4-}$ octahedra along the *c*-axis separated by cesium.[46] To investigate the morphology, microstructure, and element composition, transmission electron microscopy (TEM), high-resolution TEM (HRTEM), energy dispersive X-ray (EDX) mapping, and scanning electron microscopy (SEM) of the optimal $CsCu_2I_3$ NCs were obtained. The optimal $CsCu_2I_3$ NCs exhibit a uniform cubic-like morphology (1−2 μm) with multilayer structure (Figure 1d and Figure S2), and lattice fringes with a spacing of 0.824 nm can be observed clearly (Figure 1e), corresponding to the (110) plane of $CsCu_2I_3$ NCs. The corresponding constituent elements of Cs, Cu, and I are uniformly distributed (Figure 1f), and the atomic ratio is 1.0:2.1:3.0 as revealed by quantitative analysis (Figure S3), consistent with the ideal stoichiometric ratio of $CsCu_2I_3$, demonstrating the successful preparation of pure-phase $CsCu_2I_3$ NCs. Besides, the X-ray photoelectron spectroscopy (XPS) test was also conducted to prove that the Cu element existed as Cu^+ rather than Cu^{2+}, and no Mn element was incorporated in the optimal $CsCu_2I_3$ NCs (Figure S4). The obtained ICP-AES data of the optimal $CsCu_2I_3$ NCs (see Table S1) also demonstrates that no Mn element exists in the as-prepared $CsCu_2I_3$ NCs.

3.2. Photoluminescence Properties. Figure 2 presents the photoluminescence properties of the optimal $CsCu_2I_3$ NCs. The as-prepared $CsCu_2I_3$ NCs exhibit a strong PL emission centered at 580 nm and an excitonic absorption centered at 330 nm (Figure 2a).[46] Thus, a large Stokes shift of 250 nm is calculated for optimal $CsCu_2I_3$ NCs. Such a large Stokes shift suggests negligible self-absorption, which is extremely beneficial to the luminous performance of the optimal $CsCu_2I_3$ NCs since

https://doi.org/10.1021/acs.inorgchem.3c03724
Inorg. Chem. 2023, 62, 19848−19855

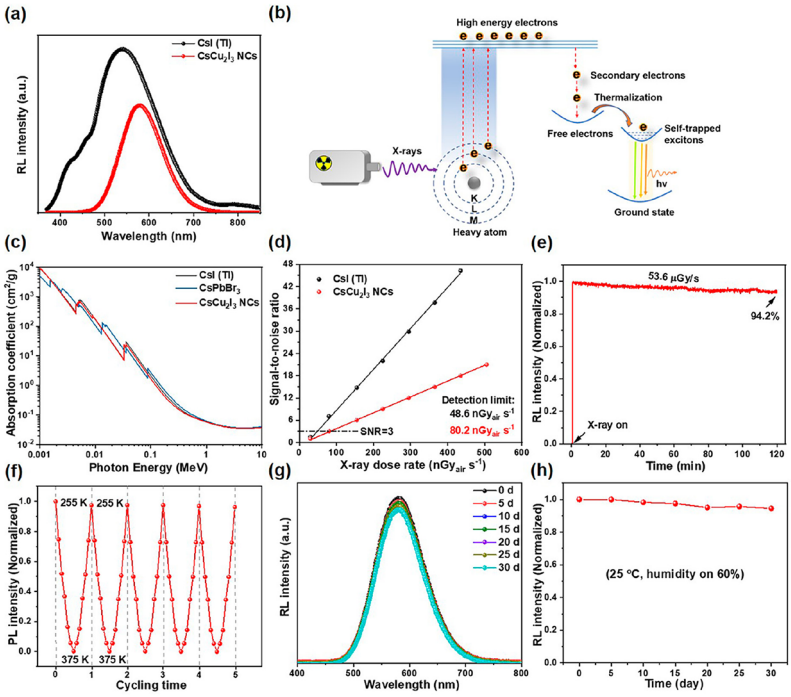

Figure 3. X-ray scintillation properties. (a) RL intensity of $CsCu_2I_3$ NCs and CsI(Tl) with the same dose rate. (b) Proposed radioluminescence mechanism. (c) Absorption coefficients of CsI(Tl), $CsPbBr_3$, and $CsCu_2I_3$ NCs. (d) Signal-to-noise ratio versus X-ray dose rate of $CsCu_2I_3$ NCs and CsI(Tl). (e) Normalized RL intensity of $CsCu_2I_3$ NCs under continuous X-ray irradiation. (f) Normalized PL intensity of $CsCu_2I_3$ NCs during five cycles of heating/cooling from 255 to 375 K. (g) RL intensity at different storage periods. (h) Normalized RL intensity of the stored (in air for 30 days) $CsCu_2I_3$ NCs.

self-absorption will seriously affect the luminous efficiency of scintillators. The CIE 1931 chromaticity coordinate of the optimal $CsCu_2I_3$ NCs is (0.39, 0.45) (Figure 2b), displaying standard yellow-light emission. The PLQY of the optimal $CsCu_2I_3$ NCs is calculated to be 61.9% (Figure 2c), which is a record-high value of the reported $CsCu_2I_3$ and is comparable to that of the best of the all-inorganic yellow-emitting lead halide perovskites (see Table S2), demonstrating the superior emission performance of the as-prepared samples. The PLQYs of other obtained NCs samples are much lower than that of the optimal $CsCu_2I_3$ NCs (Figure S5), demonstrating that the optimal $CsCu_2I_3$ NCs with pure-phase and fewer defects could exhibit more efficient PL performance due to the reduced nonradiative recombination of excitons. Then, as seen from the time-resolved PL (TRPL) decay curve result measured at 580 nm, the exciton lifetime of the optimal $CsCu_2I_3$ NCs is calculated to be 58.92 ns (Figure 2d), which is consistent with previous reports.[37] The TRPL decay curves of all perovskite NCs samples synthesized with different amounts of Mn^{2+} additive could also be well-fitted by a single exponential attenuation equation (Figure S6). With the increase of Mn^{2+} content from 0.00 to 0.02 mmol, the fluorescence lifetime shows an increasing trend. It reaches the maximum value when the Mn^{2+} content is 0.02 mmol. However, it can be observed that the lifetime of $CsCu_2I_3$ NCs is slightly shortened when the Mn^{2+} amount exceeds 0.02 mmol. This phenomenon could be ascribed to the fact that excessive Mn^{2+} can destroy the surface of $CsCu_2I_3$ NCs via detaching the OA/OAm ligands off the NCs surface, leading to the exposure of more surface defects and the reduction of fluorescence lifetime.

To explore the fluorescence origin of the optimal $CsCu_2I_3$ NCs, we investigated wavelength-dependent PL excitation (PLE) and emission spectra. As presented in Figure 2e, the line shape and peak position of the PLE spectra at different emission wavelengths (460−620 nm) remain almost the same. Besides, the PL spectra at different excitation wavelengths (250−350 nm) also exhibit an identical line shape and emission peak (Figure 2f). Thus, it can be concluded that the PL emission derives from the recombination of an identical excited state, and the possible defect emission could be excluded.[47] The large Stokes shift (~250 nm), high PLQY (61.9%) and relatively long fluorescence lifetime (58.92 ns) of the optimal $CsCu_2I_3$ NCs suggest that the STEs are the most likely origin of the PL emission.[48]

To further investigate the PL process, temperature-dependent PL spectra of the optimal $CsCu_2I_3$ NCs were also obtained. As exhibited in Figure 2g, the full width at half-maximum (FWHM) decreases with the PL intensity increasing monotonously when the temperature drops from 355 to 255 K. This phenomenon is consistent with materials whose PL emission derives from STEs.[45] It could be attributed to the gradually weakened nonradiative recombination and electron−phonon coupling as the temperature drops. Besides, no other emission peaks related to heat-induced defects can be observed, indicating good thermal stability of the as-prepared optimal $CsCu_2I_3$ NCs. Figure 2h exhibits the normalized PL intensity (I) versus the temperature (T), from which the exciton binding energy (E_a) of the optimal $CsCu_2I_3$ NCs can be fitted and calculated via Equation 1:

$$I(T) = \frac{I_0}{1 + A\exp(-E_a/k_BT)} \quad (1)$$

where I_0 is the I at T = 0 K; A is a fitting coefficient; k_B is the Boltzmann constant. The E_a of the optimal $CsCu_2I_3$ NCs is fitted to be 336 meV, which significantly exceeds the value (20−75

https://doi.org/10.1021/acs.inorgchem.3c03724
Inorg. Chem. 2023, 62, 19848−19855

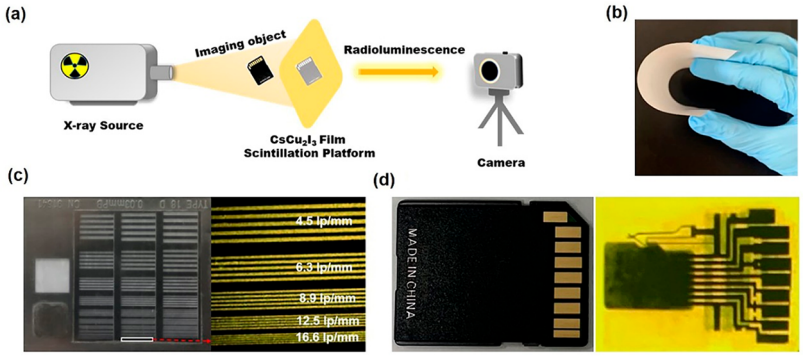

Figure 4. (a) Schematic illustration of the home-designed X-ray imaging system. (b) Photograph of the flexible $CsCu_2I_3$ NCs scintillation film. (c) Photograph (left) and X-ray image (right) of a standard X-ray test-pattern plate based on the flexible $CsCu_2I_3$ NCs film. (d) Photograph (left) and the corresponding X-ray image (right) of a SD card.

meV) of $CsPbX_3$ NCs.[22] The large E_a values of the optimal $CsCu_2I_3$ NCs can be attributed to the strong exciton confinement of their unique 1D structure. Such a large E_a could ensure the stable existence of excitons in the optimal $CsCu_2I_3$ NCs for efficient PL emission. Moreover, the FWHM versus the temperature (T) was described via the Huang−Rhys model to further investigate the electron−phonon coupling strength (as presented in Figure 2i). Equation 2 shows the Huang−Rhys equation:

$$\mathrm{FWHM} = 2.36\sqrt{S}\,\hbar\omega_{\mathrm{phonon}}\sqrt{\coth\frac{\hbar\omega_{\mathrm{phonon}}}{2k_{\mathrm{B}}T}} \quad (2)$$

where the S factor is the parameter describing the electron−phonon coupling strength, $\hbar\omega_{\mathrm{phonon}}$ is the phonon frequency ($\hbar$, Planck constant), and k_{B} is the Boltzmann constant. The calculated S factor and $\hbar\omega_{\mathrm{phonon}}$ of the optimal $CsCu_2I_3$ NCs are 38.6 and 19.8 meV, respectively. The S factor of the optimal $CsCu_2I_3$ NCs dramatically exceeds that of $CsPbX_3$ NCs, indicating that the optimal $CsCu_2I_3$ NCs have a stronger electron−phonon coupling.[49] Considering that the fitted $\hbar\omega_{\mathrm{phonon}}$ (19.8 meV) is very close to that of the reported Cs-based perovskite, the above fittings can be regarded as reliable. The relatively long fluorescence lifetime, big S factor, and large Stokes shift of the optimal $CsCu_2I_3$ NCs figure out that the PL originates from STEs.

3.3. X-ray Scintillation Properties and Mechanism. Then, the X-ray scintillation properties of the optimal $CsCu_2I_3$ NCs were also studied. Consistent with the PL emission (shown in Figure 2a), the optimal $CsCu_2I_3$ NCs also exhibit a broadband RL emission that peaked at 580 nm (Figure 3a), suggesting an identical RL mechanism. As a reference, the RL spectrum of CsI (Tl) (54000 photons MeV^{-1}) can also be found in Figure 3a. Consequently, the LY of the optimal $CsCu_2I_3$ NCs is determined to be 32000 photons MeV^{-1} via integrating the peak area, which significantly exceeds the typical commercial BGO scintillator (~8000 photons MeV^{-1}) and is superior to the commercial LYSO scintillator (20000−30000 photons MeV^{-1}) or the reported $CsPbBr_3$ NCs scintillator (30000 photons MeV^{-1}).[50] As far as we know, the calculated LY in this work is the highest value among the reported $CsCu_2I_3$ scintillators. The proposed RL scintillation process of the optimal $CsCu_2I_3$ NCs is shown in Figure 3b. First, the electrons in the inner shells of the heavy atoms of $CsCu_2I_3$ NCs were excited to higher energy levels under X-ray irradiation. Then, the high-energy electrons avalanched, generating tremendous secondary electrons. Subsequently, the secondary electrons turned into free electrons via thermalization and further transformed into STEs. Finally, the STEs underwent rapid radiative recombination, and RL was generated. Figure 3c displays the absorption coefficient curves of typical CsI (Tl), $CsPbBr_3$ and the optimal $CsCu_2I_3$ NCs scintillators at different photon energies based on a web database.[51] It can be observed that the optimal $CsCu_2I_3$ NCs present stronger X-ray absorption capacity than does $CsPbBr_3$ and are comparable to CsI (Tl). The strong X-ray absorption of the $CsCu_2I_3$ NCs benefits its excellent RL performance. Then, the RL intensity of the optimal $CsCu_2I_3$ NCs at different X-ray dose rates was obtained to investigate their sensitivity. The signal-to-noise ratio (SNR) of the NCs exhibits good linearity with the X-ray dose rates (Figure 3d). Thus, an ultralow detection limit of 80.2 nGy_{air} s^{-1} (when the SNR is 3) is determined for the optimal $CsCu_2I_3$ NCs. This detection limit is far below the value required for a medical diagnosis (5.5 μGy_{air} s^{-1}). In addition, the RL intensity of the optimal $CsCu_2I_3$ NCs was maintained at 94.2% after 120 min continuous X-ray irradiation (53.6 μGy s^{-1}), demonstrating excellent stability against X-ray irradiation (Figure 3e). We also recorded the PL intensity of the optimal $CsCu_2I_3$ NCs during five cycles of heating/cooling from 255 to 375 K to evaluate the thermal stability. Surprisingly, the PL intensity of the recycled $CsCu_2I_3$ NCs was maintained at 95% (Figure 3f). Besides, the XRD pattern and TEM image of the recycled $CsCu_2I_3$ NCs were almost unchanged (Figure S7), demonstrating the excellent thermal stability, which also could be confirmed by the thermogravimetric analysis result (Figure S8). We monitored the RL intensity of the optimal $CsCu_2I_3$ NCs (25 °C, humidity of 60%) for 30 days to evaluate their storage stability. As exhibited in Figure 3g,h, the RL intensity of the stored (in the air for 30 days) $CsCu_2I_3$ NCs maintained at >90% of the original value. Moreover, the XRD pattern of the stored optimal $CsCu_2I_3$ NCs was almost unchanged (Figure S9), indicating the superior storage stability of the as-prepared $CsCu_2I_3$ NCs.

3.4. X-ray Imaging Performance. Eventually, a home-designed X-ray imaging system was developed to investigate the practical X-ray imaging performance of optimal $CsCu_2I_3$ NCs. Figure 4a exhibits the placing order of the X-ray source, imaging object, $CsCu_2I_3$ NCs scintillator film, and camera in the imaging process. It is worth noting that good bendability was obtained for the scintillator film coated on the PVC flexible substrate (Figure 4b). To evaluate the imaging quality, we investigated the spatial resolution of the scintillator film by obtaining an X-ray image of a standard X-ray test-pattern plate. The $CsCu_2I_3$ NCs

https://doi.org/10.1021/acs.inorgchem.3c03724
Inorg. Chem. 2023, 62, 19848−19855

scintillator film displayed a spatial resolution of 16.6 lp mm^{-1} (Figure 4c), which exceeds most commercial inorganic scintillators and the reported lead-based perovskite scintillators,[52] demonstrating the great potential of the $CsCu_2I_3$ NCs for high-resolution X-ray imaging. Figure 4d exhibits the X-ray image of an SD card obtained from the homemade imaging system. The internal construction of the SD card, which is opaque to visible light, can be observed clearly from the captured X-ray image, suggesting the excellent X-ray imaging performance of optimal $CsCu_2I_3$ NCs.

4. CONCLUSIONS

In summary, efficient yellow emissive $CsCu_2I_3$ NCs with single-phase purity and few defects were prepared via a simple Mn^{2+}-assisted hot-injection method. It is found that adding a small amount of Mn^{2+} could effectively induce the phase transformation from $Cs_3Cu_2I_5$ to $CsCu_2I_3$, leading to the preparation of pure-phase $CsCu_2I_3$ NCs with few defects and high fluorescence performance. The as-prepared "optimal $CsCu_2I_3$ NCs" exhibited superior PL performance with a record-high PLQY of 61.9%. The fluorescence derived from the strongly localized 1D STEs emission, which was systematically investigated via the wavelength-dependent PL excitation, PL emission, and the temperature-dependent PL spectra. Remarkably, the $CsCu_2I_3$ NCs also exhibited amazing scintillation properties with a high LY (32000 photons MeV^{-1}) and an ultralow detection limit (80.2 nGy_{air} s^{-1}). Eventually, the $CsCu_2I_3$ NCs scintillator film demonstrated an ultrahigh spatial resolution (16.6 lp mm^{-1}) in X-ray imaging. Good stabilities against X-ray irradiation, heat, and environmental storage were also achieved for the $CsCu_2I_3$ NCs. The work suggests the vast application potential of $CsCu_2I_3$ NCs in flexible X-ray detection and imaging.

■ ASSOCIATED CONTENT

Supporting Information

The Supporting Information is available free of charge at https://pubs.acs.org/doi/10.1021/acs.inorgchem.3c03724.

Additional details of experimental section, schematic of synthesis process, quantitative analysis, XPS analysis, PLQY measurement, TRPL analysis, XRD pattern, SEM analysis, thermogravimetric analysis, ICP-AES test and summarization of all-inorganic yellow-light-emitting halide compounds with high PLQY (PDF)

■ AUTHOR INFORMATION

Corresponding Author

Yu Wang − *SZU-NUS Collaborative Innovation Center for Optoelectronic Science & Technology, International Collaborative Laboratory of 2D Materials for Optoelectronics Science and Technology of Ministry of Education, Institute of Microscale Optoelectronics, Shenzhen University, Shenzhen 518060, China;* orcid.org/0000-0001-5971-6597; Email: wangyu@szu.edu.cn

Authors

Lingfeng Li − *SZU-NUS Collaborative Innovation Center for Optoelectronic Science & Technology, International Collaborative Laboratory of 2D Materials for Optoelectronics Science and Technology of Ministry of Education, Institute of Microscale Optoelectronics, Shenzhen University, Shenzhen 518060, China*

Zutao Fan − *SZU-NUS Collaborative Innovation Center for Optoelectronic Science & Technology, International Collaborative Laboratory of 2D Materials for Optoelectronics Science and Technology of Ministry of Education, Institute of Microscale Optoelectronics, Shenzhen University, Shenzhen 518060, China*

Jie Zhang − *SZU-NUS Collaborative Innovation Center for Optoelectronic Science & Technology, International Collaborative Laboratory of 2D Materials for Optoelectronics Science and Technology of Ministry of Education, Institute of Microscale Optoelectronics, Shenzhen University, Shenzhen 518060, China*

Dianyuan Fan − *SZU-NUS Collaborative Innovation Center for Optoelectronic Science & Technology, International Collaborative Laboratory of 2D Materials for Optoelectronics Science and Technology of Ministry of Education, Institute of Microscale Optoelectronics, Shenzhen University, Shenzhen 518060, China*

Xiaogang Liu − *SZU-NUS Collaborative Innovation Center for Optoelectronic Science & Technology, International Collaborative Laboratory of 2D Materials for Optoelectronics Science and Technology of Ministry of Education, Institute of Microscale Optoelectronics, Shenzhen University, Shenzhen 518060, China; Department of Chemistry, National University of Singapore, Singapore 117543, Singapore;* orcid.org/0000-0003-2517-5790

Complete contact information is available at: https://pubs.acs.org/10.1021/acs.inorgchem.3c03724

Notes

The authors declare no competing financial interest.

■ ACKNOWLEDGMENTS

We acknowledge the Science and Technology Project of Shenzhen (grant no. JCYJ20220531102603007) for financial support. The authors acknowledge the assistance of the Instrumental Analysis Center of Shenzhen University (Lihu Campus) for TEM imaging and PL measurements.

■ REFERENCES

(1) Yaffe, M. J.; Rowlands, J. A. X-ray detectors for digital radiography. *Phys. Med. Biol.* **1997**, *42*, 1.

(2) Weber, M. J. Inorganic scintillators: Today and tomorrow. *J. Lumin.* **2002**, *100*, 35−45.

(3) Büchele, P.; Richter, M.; Tedde, S. F.; Matt, G. J.; Ankah, G. N.; Fischer, R.; Biele, M.; Metzger, W.; Lilliu, S.; Bikondoa, O.; Macdonald, J. E.; Brabec, C. J.; Kraus, T.; Lemmer, U.; Schmidt, O. X-ray imaging with scintillator-sensitized hybrid organic photodetectors. *Nat. Photonics* **2015**, *9*, 843−848.

(4) Zhuravleva, M.; Friedrich, S.; Melcher, C. L. Praseodymium valence determination in Lu_2SiO_5, Y_2SiO_5, and $Lu_3Al_5O_{12}$ scintillators by X-ray absorption spectroscopy. *Appl. Phys. Lett.* **2012**, *101*, 101902.

(5) Gandini, M.; Villa, I.; Beretta, M.; Gotti, C.; Imran, M.; Carulli, F.; Fantuzzi, E.; Sassi, M.; Zaffalon, M.; Brofferio, C.; Manna, L.; Beverina, L.; Vedda, A.; Fasoli, M.; Gironi, L.; Brovelli, S. Efficient, fast and reabsorption-free perovskite nanocrystal-based sensitized plastic scintillators. *Nat. Nanotechnol.* **2020**, *15*, 462−468.

(6) Zhao, J.; Zhao, L.; Deng, Y.; Xiao, X.; Ni, Z.; Xu, S.; Huang, J. Perovskite-filled membranes for flexible and large-area direct-conversion X-ray detector arrays. *Nat. Photonics* **2020**, *14*, 612−617.

(7) Chen, Q.; Wu, J.; Ou, X.; Huang, B.; Almutlaq, J.; Zhumekenov, A. A.; Guan, X.; Han, S.; Liang, L.; Yi, Z.; Li, J.; Xie, X.; Wang, Y.; Li, Y.; Fan, D.; Teh, D. B. L.; All, A. H.; Mohammed, O. F.; Bakr, O. M.; Wu,

T.; Bettinelli, M.; Yang, H.; Huang, W.; Liu, X. All-inorganic perovskite nanocrystal scintillators. *Nature* **2018**, *561*, 88−93.
(8) Nikl, M.; Yoshikawa, A. Recent R&D trends in inorganic single-crystal scintillator materials for radiation detection. *Adv. Opt. Mater.* **2015**, *3*, 463−481.
(9) Daneshi, I.; Mohammadzadeh, M. Design and fabrication of a CsI (Tl) micro-columnar structure scintillation film for digital dental radiography application. *J. Instrum.* **2019**, *14*, P10039.
(10) Qin, L.; Li, H.; Lu, S.; Ding, D.; Ren, G. Growth and characteristics of LYSO ($Lu_{2(1-x-y)}Y_{2x}SiO_5:Ce_y$) scintillation crystals. *J. Cryst. Growth* **2005**, *281*, 518−524.
(11) Feng, H.; Jary, V.; Mihokova, E.; Ding, D.; Nikl, M.; Ren, G.; Li, H.; Pan, S.; Beitlerova, A.; Kucerkova, R. Temperature dependence of luminescence characteristics of $Lu_{2(1-x)}Y_{2x}SiO_5:Ce^{3+}$ scintillator grown by the Czochralski method. *J. Appl. Phys.* **2010**, *108*, 033519.
(12) Yawai, N.; Chewpraditkul, W.; Wanarak, C.; Nikl, M.; Ratanatongchai, W. Intrinsic light yield and light loss coefficient of $Bi_4Ge_3O_{12}$ single crystals. *Opt. Mater.* **2014**, *36*, 2030−2033.
(13) Mao, P.; Tang, Y.; Wang, B.; Fan, D.; Wang, Y. Organic-inorganic hybrid cuprous halide scintillators for flexible X-ray imaging. *ACS Appl. Mater. Interfaces* **2022**, *14*, 22295−22301.
(14) Zhou, Q.; Ren, J.; Xiao, J.; Lei, L.; Liao, F.; Di, H.; Wang, C.; Yang, L.; Chen, Q.; Yang, X.; Zhao, Y.; Han, X. Highly efficient copper halide scintillators for high-performance and dynamic X-ray imaging. *Nanoscale* **2021**, *13*, 19894−19902.
(15) Heo, J. H.; Shin, D. H.; Park, J. K.; Kim, D. H.; Lee, S. J.; Im, S. H. High-performance next-generation perovskite nanocrystal scintillator for nondestructive X-ray imaging. *Adv. Mater.* **2018**, *30*, 1801743.
(16) Liu, J.; Shabbir, B.; Wang, C.; Wan, T.; Ou, Q.; Yu, P.; Tadich, A.; Jiao, X.; Chu, D.; Qi, D.; Li, D.; Kan, R.; Huang, Y.; Dong, Y.; Jasieniak, J.; Zhang, Y.; Bao, Q. Flexible, printable soft-X-ray detectors based on all-inorganic perovskite quantum dots. *Adv. Mater.* **2019**, *31*, 1901644.
(17) Zhang, Y.; Sun, R.; Ou, X.; Fu, K.; Chen, Q.; Ding, Y.; Xu, L.-J.; Liu, L.; Han, Y.; Malko, A. V.; Liu, X.; Yang, H.; Bakr, O. M.; Liu, H.; Mohammed, O. F. Metal halide perovskite nanosheet for X-ray high-resolution scintillation imaging screens. *ACS Nano* **2019**, *13*, 2520−2525.
(18) Cao, F.; Yu, D.; Ma, W.; Xu, X.; Cai, B.; Yang, Y. M.; Liu, S.; He, L.; Ke, Y.; Lan, S.; Choy, K.-L.; Zeng, H. Shining emitter in a stable host: Design of halide perovskite scintillators for X-ray imaging from commercial concept. *ACS Nano* **2020**, *14*, 5183−5193.
(19) Zhou, Y.; Chen, J.; Bakr, O. M.; Mohammed, O. F. Metal halide perovskites for X-ray imaging scintillators and detectors. *ACS Energy Lett.* **2021**, *6*, 739−768.
(20) Shrestha, S.; Fischer, R.; Matt, G. J.; Feldner, P.; Michel, T.; Osvet, A.; Levchuk, I.; Merle, B.; Golkar, S.; Chen, H.; Tedde, S. F.; Schmidt, O.; Hock, R.; Rührig, M.; Göken, M.; Heiss, W.; Anton, G.; Brabec, C. J. High-performance direct conversion X-ray detectors based on sintered hybrid lead triiodide perovskite wafers. *Nat. Photonics* **2017**, *11*, 436−440.
(21) Wei, H.; Fang, Y.; Mulligan, P.; Chuirazzi, W.; Fang, H.-H.; Wang, C.; Ecker, B. R.; Gao, Y.; Loi, M. A.; Cao, L.; Huang, J. Sensitive X-ray detectors made of methylammonium lead tribromide perovskite single crystals. *Nat. Photonics* **2016**, *10*, 333−339.
(22) Protesescu, L.; Yakunin, S.; Bodnarchuk, M. I.; Krieg, F.; Caputo, R.; Hendon, C. H.; Yang, R. X.; Walsh, A.; Kovalenko, M. V. Nanocrystals of cesium lead halide perovskites ($CsPbX_3$, X = Cl, Br, and I): Novel optoelectronic materials showing bright emission with wide color gamut. *Nano Lett.* **2015**, *15*, 3692−3696.
(23) Chen, W.; Liu, Y.; Yuan, Z.; Xu, Z.; Zhang, Z.; Liu, K.; Jin, Z.; Tang, X. X-ray radioluminescence effect of all-inorganic halide perovskite $CsPbBr_3$ quantum dots. *J. Radioanal. Nucl. Ch.* **2017**, *314*, 2327−2337.
(24) Wei, J.-H.; Liao, J.-F.; Wang, X.-D.; Zhou, L.; Jiang, Y.; Kuang, D.-B. All-inorganic lead-free heterometallic $Cs_4MnBi_2Cl_{12}$ perovskite single crystal with highly efficient orange emission. *Matter* **2020**, *3*, 892−903.
(25) Zhu, W.; Ma, W.; Su, Y.; Chen, Z.; Chen, X.; Ma, Y.; Bai, L.; Xiao, W.; Liu, T.; Zhu, H.; Liu, X.; Liu, H.; Liu, X.; Yang, Y. Low-dose real-time X-ray imaging with nontoxic double perovskite scintillators. *Light-Sci. Appl.* **2020**, *9*, 112.
(26) Zhao, X.; Niu, G.; Zhu, J.; Yang, B.; Yuan, J.-H.; Li, S.; Gao, W.; Hu, Q.; Yin, L.; Xue, K.-H.; Lifshitz, E.; Miao, X.; Tang, J. All-inorganic copper halide as a stable and self-absorption-free X-ray scintillator. *J. Phys. Chem. Lett.* **2020**, *11*, 1873−1880.
(27) Gao, W.; Niu, G.; Yin, L.; Yang, B.; Yuan, J.-H.; Zhang, D.; Xue, K.-H.; Miao, X.; Hu, Q.; Du, X.; Tang, J. One-dimensional all-inorganic K_2CuBr_3 with violet emission as efficient X-ray scintillators. *ACS Appl. Electron. Mater.* **2020**, *2*, 2242−2249.
(28) Jun, T.; Sim, K.; Iimura, S.; Sasase, M.; Kamioka, H.; Kim, J.; Hosono, H. Lead-free highly efficient blue-emitting $Cs_3Cu_2I_5$ with 0D electronic structure. *Adv. Mater.* **2018**, *30*, 1804547.
(29) Lian, L.; Zheng, M.; Zhang, W.; Yin, L.; Du, X.; Zhang, P.; Zhang, X.; Gao, J.; Zhang, D.; Gao, L.; Niu, G.; Song, H.; Chen, R.; Lan, X.; Tang, J.; Zhang, J. Efficient and reabsorption-free radioluminescence in $Cs_3Cu_2I_5$ nanocrystals with self-trapped excitons. *Adv. Sci.* **2020**, *7*, 2000195.
(30) Cheng, S.; Beitlerova, A.; Kucerkova, R.; Nikl, M.; Ren, G.; Wu, Y. Zero-dimensional $Cs_3Cu_2I_5$ perovskite single crystal as sensitive X-ray and γ-ray scintillator. *phys. status solidi-R.* **2020**, *14*, 2000374.
(31) Yuan, D. Air-stable bulk halide single-crystal scintillator $Cs_3Cu_2I_5$ by melt growth: Intrinsic and Tl doped with high light yield. *ACS Appl. Mater. Interfaces* **2020**, *12*, 38333−38340.
(32) Ma, Z.; Shi, Z.; Yang, D.; Li, Y.; Zhang, F.; Wang, L.; Chen, X.; Wu, D.; Tian, Y.; Zhang, Y.; Zhang, L.; Li, X.; Shan, C. High color-rendering index and stable white light-emitting diodes by assembling two broadband emissive self-trapped excitons. *Adv. Mater.* **2021**, *33*, 2001367.
(33) Li, J.; Inoshita, T.; Ying, T.; Ooishi, A.; Kim, J.; Hosono, H. A highly efficient and stable blue-emitting $Cs_5Cu_3Cl_6I_2$ with a 1D chain structure. *Adv. Mater.* **2020**, *32*, 2002945.
(34) Shen, D.; Wang, X.; Zhang, X.; Liu, Y.; Shi, Y.; Li, X.; Chen, X.; Zhang, Y. Real-time observation of anion-exchange reaction in $Cs_3Cu_2Cl_5$ single crystal. *ACS Appl. Opt. Mater.* **2023**, *1*, 435−441.
(35) Yang, B.; Yin, L.; Niu, G.; Yuan, J.-H.; Xue, K.-H.; Tan, Z.; Miao, X.-S.; Niu, M.; Du, X.; Song, H.; Lifshitz, E.; Tang, J. Lead-free halide Rb_2CuBr_3 as sensitive X-ray scintillator. *Adv. Mater.* **2019**, *31*, 1904711.
(36) Hull, S.; Berastegui, P. Crystal structures and ionic conductivities of ternary derivatives of the silver and copper monohalides-II: Ordered phases within the $(AgX)_x$-$(MX)_{1-x}$ and $(CuX)_x$-$(MX)_{1-x}$ (M = K, Rb and Cs; X═Cl, Br and I) systems. *J. Solid State Chem.* **2004**, *177*, 3156−3173.
(37) Lin, R.; Guo, Q.; Zhu, Q.; Zhu, Y.; Zheng, W.; Huang, F. All-inorganic $CsCu_2I_3$ single crystal with high-PLQY (≈15.7%) intrinsic white-light emission via strongly localized 1D excitonic recombination. *Adv. Mater.* **2019**, *31*, 1905079.
(38) Cheng, P.; Sun, L.; Feng, L.; Yang, S.; Yang, Y.; Zheng, D.; Zhao, Y.; Sang, Y.; Zhang, R.; Wei, D.; Deng, W.; Han, K. Colloidal synthesis and optical properties of all-inorganic low-dimensional cesium copper halide nanocrystals. *Angew. Chem., Int. Ed.* **2019**, *58*, 16087−16091.
(39) Xing, Z.; Zhou, Z.; Zhong, G.; Chan, C. C. S.; Li, Y.; Zou, X.; Halpert, J. E.; Su, H.; Wong, K. S. Barrierless exciton self-trapping and emission mechanism in low-dimensional copper halides. *Adv. Funct. Mater.* **2022**, *32*, 2207638.
(40) Zhang, M.; Zhu, J.; Yang, B.; Niu, G.; Wu, H.; Zhao, X.; Yin, L.; Jin, T.; Liang, X.; Tang, J. Oriented-structured $CsCu_2I_3$ film by close-space sublimation and nanoscale seed screening for high-resolution X-ray imaging. *Nano Lett.* **2021**, *21*, 1392−1399.
(41) Cheng, S.; Beitlerova, A.; Kucerkova, R.; Mihokova, E.; Nikl, M.; Zhou, Z.; Ren, G.; Wu, Y. Non-hygroscopic, self-absorption free, and efficient 1D $CsCu_2I_3$ perovskite single crystal for radiation detection. *ACS Appl. Mater. Interfaces* **2021**, *13*, 12198−12202.
(42) Mo, X.; Li, T.; Huang, F.; Li, Z.; Zhou, Y.; Lin, T.; Ouyang, Y.; Tao, X.; Pan, C. Highly-efficient all-inorganic lead-free 1D $CsCu_2I_3$ single crystal for white-light emitting diodes and UV photodetection. *Nano Energy* **2021**, *81*, 105570.
(43) Gao, F.; Yang, W.; Liu, X.; Li, Y.; Liu, W.; Xu, H.; Liu, Y. Highly stable and luminescent silica-coated perovskite quantum dots at

https://doi.org/10.1021/acs.inorgchem.3c03724
Inorg. Chem. 2023, 62, 19848−19855

nanoscale-particle level via nonpolar solvent synthesis. *Chem. Eng. J.* **2021**, *407*, 128001.
(44) Fan, R.; Fang, S.; Liang, C.; Liang, Z.; Zhong, H. Controllable one-step doping synthesis for the white-light emission of cesium copper iodide perovskites. *Photon. Res.* **2021**, *9*, 694−700.
(45) Gao, F.; Zhu, X.; Feng, Q.; Zhong, W.; Liu, W.; Xu, H.; Liu, Y. Deep-blue emissive $Cs_3Cu_2I_5$ perovskites nanocrystals with 96.6% quantum yield via InI_3-assisted synthesis for light-emitting device and fluorescent ink applications. *Nano Energy* **2022**, *98*, 107270.
(46) Vashishtha, P.; Nutan, G. V. E.; Griffith, B.; Fang, Y.; Giovanni, D.; Jagadeeswararao, M.; Sum, T. C.; Mathews, N.; Mhaisalkar, S. G.; Hanna, J. V.; White, T. Cesium copper iodide tailored nanoplates and nanorods for blue, yellow, and white emission. *Chem. Mater.* **2019**, *31*, 9003−9011.
(47) Luo, J.; Wang, X.; Li, S.; Liu, J.; Guo, Y.; Niu, G.; Yao, L.; Fu, Y.; Gao, L.; Dong, Q.; Zhao, C.; Leng, M.; Ma, F.; Liang, W.; Wang, L.; Jin, S.; Han, J.; Zhang, L.; Etheridge, J.; Wang, J.; Yan, Y.; Sargent, E. H.; Tang, J. Efficient and stable emission of warm-white light from lead-free halide double perovskites. *Nature* **2018**, *563*, 541−545.
(48) Li, S.; Luo, J.; Liu, J.; Tang, J. Self-trapped excitons in all-inorganic halide perovskites: Fundamentals, status, and potential applications. *J. Phys. Chem. Lett.* **2019**, *10*, 1999−2007.
(49) Lao, X.; Yang, Z.; Su, Z.; Bao, Y.; Zhang, J.; Wang, X.; Cui, X.; Wang, M.; Yao, X.; Xu, S. Anomalous temperature-dependent exciton-phonon coupling in cesium lead bromide perovskite nanosheets. *J. Phys. Chem. C* **2019**, *123*, 5128−5135.
(50) Chen, H.; Wang, Q.; Peng, G.; Wang, S.; Lei, Y.; Wang, H.; Yang, Z.; Sun, J.; Li, N.; Zhao, L.; Lan, W.; Jin, Z. Cesium lead halide nanocrystals based flexible X-ray imaging screen and visible dose rate indication on paper substrate. *Adv. Opt. Mater.* **2022**, *10*, 2102790.
(51) National Institute of Standards and Technology. Physical Reference Data. https://www.physics.nist.gov/PhysRefData/Xcom/html/xcom1.html (accessed on Oct, 2021).
(52) Wang, Z.; Wei, Y.; Liu, C.; Liu, Y.; Hong, M. Mn^{2+}-activated $Cs_3Cu_2I_5$ nano-scintillators for ultra-high resolution flexible X-ray imaging. *Laser Photonics Rev.* **2023**, *17*, 2200851.

https://doi.org/10.1021/acs.inorgchem.3c03724
Inorg. Chem. 2023, 62, 19848−19855